

ARTICLE OPEN



ENSO-driven abrupt phase shift in North Atlantic oscillation in early January

Xin Geng^{1,2}, Jiuwei Zhao¹ and Jong-Seong Kug^{1,2,3}✉

El Niño–Southern Oscillation (ENSO) teleconnections exhibit a strong dependency on seasonally and intraseasonally varying mean states, leading to impactful short-term variations in regional climate. The North Atlantic Oscillation (NAO)–ENSO relation is a typical example, in that its phase relationship reverses systematically between the early and late winter. Here based on observations and an ensemble of atmosphere-only climate model simulations, we reveal that this NAO phase reversal occurs synchronously in early January, showing strong abruptness. We demonstrate that this abrupt NAO phase reversal is caused by the change in ENSO-induced Rossby wave-propagating direction from northeastward to southeastward over the northeastern North American region, which is largely governed by a climatological alteration of the local jet meridional shear. We also provide evidence that the North Atlantic intrinsic eddy–low-frequency flow feedback further amplifies the NAO responses. This ENSO-related abrupt NAO change offers an avenue for intraseasonal climate forecasting in the Euro-Atlantic region.

npj Climate and Atmospheric Science (2023)6:80; <https://doi.org/10.1038/s41612-023-00414-2>

INTRODUCTION

As the most consequential mode of interannual climate variability, the El Niño–Southern Oscillation (ENSO)¹ triggers pronounced impacts on weather and climate around the globe². Although climate responses in the North Pacific and North America have been relatively well understood^{3–5}, the ENSO effects on circulation over the remote Euro-Atlantic sector are more controversial⁶. Early studies argued that no evident ENSO-related climate traces could be detected there^{7,8}. However, many subsequent observational diagnoses and modeling experiments suggested that ENSO footprints do exist over the Euro-Atlantic sector but exhibit highly asymmetric and nonstationary features^{9,10}. For example, the teleconnection undergoes substantial intraseasonal variations from November to March^{11–13}. In early winter (November–December), the response to a warm ENSO event features a negative geopotential height anomaly in the northern North Atlantic and a positive anomaly in the south, which spatially projects onto a positive phase of the North Atlantic Oscillation (NAO)^{12,14,15}. As the center of the anomaly is shifted slightly southward relative to the NAO pattern, some studies also refer to it as a positive phase of the East Atlantic pattern^{16,17}. In late winter (January–March), however, a pattern that manifests as an evident negative NAO phase is observed^{18,19}.

Previous studies have proposed various mechanisms for understanding these wintertime NAO responses to ENSO forcing. During an El Niño/La Niña early winter, strong convection anomalies in the tropical Indian–western Pacific Ocean^{13–15} and/or the Gulf of Mexico–Caribbean Sea^{12,20} could excite Rossby wave trains that reach the North Atlantic and then lead to a positive/negative NAO phase. However, during late winter, the linkage is more complicated. First, the decayed tropical North Atlantic (TNA) sea surface temperature (SST) anomalies in response to ENSO forcing become robust during this period and may exert a modulation effect on the NAO atmospheric circulation^{21,22}. Also, the ENSO-induced positive/negative convection anomalies in the tropical central-eastern Pacific strengthen during late winters and start

playing an overwhelming role in generating various low-frequency Rossby waves or transient eddies propagating downstream from the North Pacific to the North Atlantic, which in turn gives rise to a negative/positive NAO pattern^{19,23}. In addition, a chain of stratospheric processes emerges as another key mechanism that works together with the aforementioned tropospheric pathways^{12,19}. Under El Niño conditions, the deepened Aleutian low that is associated with the amplification of wavenumber one and enhanced wave activity upward propagation into the lower stratosphere leads to deceleration of the stratospheric polar vortex²⁴. These stratospheric circulation anomalies then propagate downward and result in a subsequent late winter-negative NAO anomaly^{18,25,26}. The opposite generally happens during La Niña conditions, particularly for strong events^{24,27}.

Despite being studied extensively, our understanding of the wintertime Euro-Atlantic atmospheric responses to ENSO on intraseasonal timescales is still immature. In particular, the previous studies concentrated mostly on the NAO responses during either the early or late winter of ENSO events. When and how this NAO phase transition occurs from December to January remains overlooked and unexplored. In the current study, using the high temporal resolution daily reanalysis datasets and abundant Atmospheric Model Intercomparison Project (AMIP) simulations that were part of the Coupled Model Intercomparison Project phase 6 (CMIP6), we reveal that the NAO response to ENSO within the boreal winter undergoes an abrupt phase reversal, which occurs synchronously in early January. A tropospheric mechanism is then proposed to physically understand this phase-locked intraseasonal ENSO teleconnection change.

RESULTS

Abrupt ENSO–NAO teleconnection reversal

We begin by examining the regressed Euro-Atlantic (70°–0°W) zonal mean daily sea-level pressure (SLP) anomalies with respect to

¹CIC-FEMD/ILCEC, Key Laboratory of Meteorological Disaster of Ministry of Education (KLME), Nanjing University of Information Science and Technology, Nanjing, China. ²Division of Environmental Science and Engineering, Pohang University of Science and Technology, Pohang, South Korea. ³Institute for Convergence Research and Education in Advanced Technology, Yonsei University, Seoul, South Korea. ✉email: jskug1@gmail.com

the Niño-3.4 index from December to January, as shown in Fig. 1a. There clearly exists a prominent NAO phase transition, from positive to negative, in early January of the ENSO warm phase winter. From December 1 to about January 5 (hereafter referred to as P1), the Euro-Atlantic region is characterized by an SLP anomaly pattern of a positive NAO phase in response to the El Niño forcing (Supplementary Fig. 1a). However, from January 10 until about January 25 (hereafter denoted as P2), the atmospheric pattern abruptly reverses its distribution with evident positive SLP anomalies in the north and negative anomalies in the south, which project onto an evident negative NAO phase (Supplementary Fig. 1b). The ENSO-regressed NAO index also shows a consistent feature, with an abrupt phase reversal, around January 8.

We then display the Euro-Atlantic SLP anomalies during the two super El Niño winters, namely the winters of 1997–98 and 2015–16. It is clear that the anomalies also exhibit an obviously strong NAO phase reversal from positive to negative in early January (Fig. 1b), consistent with the former regression results. It should be noted that we do not show the NAO anomalies during another 1982–83 super El Niño winter because there was a strong El Chichón volcanic eruption that occurred in the spring of 1982²⁸. Such an event can exert remarkable impacts on the Euro-Atlantic atmospheric circulation for about 1–2 years after the eruption^{29,30}.

To further consolidate this phenomenon, we adopt a suit of 26 AMIP-style simulations derived from CMIP6 experiments (see details in Methods) to conduct a parallel analysis. The results based on the multi-model ensemble mean (MME) are displayed in Fig. 1c. It is found that the simulated ENSO-regressed SLP pattern and NAO index also feature abrupt NAO phase transitions, from positive to negative, in early January of the El Niño winter. Even the transition timing agrees adequately with the observational

counterpart (Fig. 1c). However, given the non-negligible inter-model spreads (Supplementary Fig. 2a), we evaluated the performance of each model by comparing the ENSO-related Euro-Atlantic zonal mean (70°–0°W) daily SLP evolution pattern with the observations. We then select the ten best AMIP models (AMIP-B10) based on the pattern correlations because they consistently better reproduce this abrupt NAO phase reversal (Supplementary Fig. 2).

It is well known that the NAO is a leading atmospheric mode over the Euro-Atlantic region and is responsible for considerable local weather and climate predictability^{31,32}. The corresponding regional climate anomalies were thus examined. As expected, rapid changes in terms of the anomalous low-level winds and surface air temperatures from P1 to P2 are detected (Fig. 1d). Prominent temperature warming prevails in the regions of eastern Canada, Greenland, and North Africa, whereas strong northerly wind anomalies with rapid cooling occur in western Europe and eastern America. This is a typical climate response to a decrease in the NAO. The aforementioned results imply that this intraseasonal NAO phase reversal signal during ENSO in early January is robust enough to be applied to the operation of regional climate prediction.

Possible physical mechanisms

We now turn to explore the possible mechanisms responsible for this NAO phase reversal in response to ENSO forcing. It is unlikely that this abrupt intraseasonal ENSO teleconnection change can be explained by ENSO local SSTs because SST anomalies in the central-eastern tropical Pacific are highly persistent during the boreal winter season³³. We first examine ENSO-related

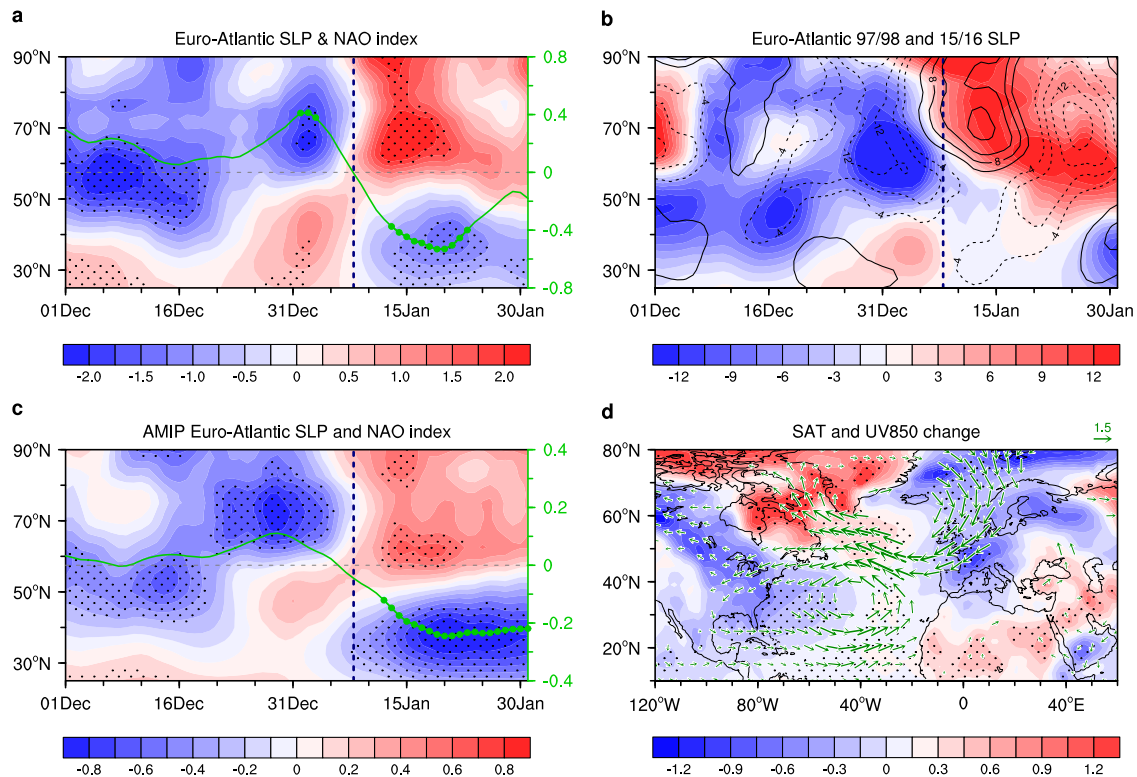


Fig. 1 An abrupt ENSO-NAO teleconnection reversal in early January. Regression coefficients of the North Atlantic zonal mean (70°–0°W) daily SLP (shadings in hPa) and NAO index (green curve) with respect to Niño-3.4 index from December to January for **a** observations and **c** the multi-model ensemble mean (MME) of the AMIP simulations. **b** The North Atlantic zonal mean (70°–0°W) daily SLP anomalies during the 1997–98 (shadings in hPa) and 2015–16 (contours in hPa) super El Niño winters. **d** Regression coefficients of observational surface air temperature (shadings in K) and 850-hPa wind (vectors in ms⁻¹) shifts from P1 (December 1 to January 5) to P2 (January 10 to 25) with respect to Niño-3.4 index. Dark blue dashed, vertical lines roughly denote the NAO phase transition timing. Dots and wind vectors are displayed only when the values are significant at the 90% confidence level (calculated using a two-tailed Student's *t*-test).

stratospheric daily anomalies because the stratosphere has been considered a major medium that leads to the late winter ENSO influence over the Euro-Atlantic sector^{18,25,26}. However, in our case, no significant stratospheric signal propagates downward to influence the troposphere during December–January (Supplementary Fig. 3a, b), which is consistent with previous studies suggesting that the stratospheric signal generally propagates downward during the midwinter and does not reach the surface until February^{18,25,26}. The earlier occurrence of the NAO phase transition in early January implies that tropospheric pathways of ENSO influence are more important¹⁹. The tropospheric processes modulated by boundary conditions are then analyzed, which mainly include a delayed local TNA SST modulation^{21,22} and/or Rossby wave trains excited by the ENSO-induced tropical convection that propagates into the Euro-Atlantic region^{12–15,20}. Unfortunately, the spatial patterns and amplitudes of ENSO-related TNA SSTs (Supplementary Fig. 3c, d) and tropical convection anomalies (Supplementary Fig. 4a, b) during P1 and P2 are quite similar. Although the amplitudes of the tropical rainfall responses show some intraseasonal variations, e.g., the convection anomalies in the central Pacific are apparently enhanced (Supplementary Fig. 4), they have the same sign of the anomaly and thus cannot directly explain the abrupt NAO phase transition from positive to negative in the early January of El Niño winter.

Next, we compare the atmospheric anomalies in the troposphere directly. Figure 2 shows the ENSO-regressed, 250-hPa geopotential height anomalies for P1 and P2. To illustrate the wave energy propagation, the associated wave activity flux (WAF) (see details in Methods) is also displayed. It can be seen that during El Niño P1, two evident Rossby wave trains propagate poleward from the tropical central Pacific and the Indo-western Pacific to the North Pacific. These wave energies continue heading northeastward across North America and then arrive in the North Atlantic region. This gives rise to the negative geopotential height anomalies around Iceland, which project onto a positive NAO

pattern (Fig. 2a). During El Niño P2, the Rossby wave train emanated from the tropical central Pacific becomes dominant. And the wave characteristics in North America–North Atlantic sector are dramatically different from those in El Niño P1. The wave energy during P2 heads southeastward rather than northeastward before it enters the North Atlantic region. This results in the negative geopotential height anomalies shifting southward from Iceland to the Azores. The shift in anomalies projects onto a negative NAO phase and is therefore responsible for the NAO phase reversal (Fig. 2b). The change in Rossby wave propagation direction from P1 to P2 is also visible in the AMIP simulations (Fig. 2c, d and Supplementary Fig. 5). Therefore, we suggest that the proximate cause of NAO phase reversal in early January during ENSO events is the Rossby wave-propagating direction change over the northeastern North American region. To determine the origin of the Rossby wave, the tropical Indo-western Pacific and central Pacific precipitation indices are defined (i.e., Pr_IOWP and Pr_CP, see details in Methods). Partial regression analysis (Supplementary Fig. 6) suggests that the Rossby wave train with different propagation directions primarily stems from the tropical central Pacific forcing. The Pr_IOWP-related Rossby wave train shows similar characteristics during P1 and P2, both projecting onto the positive phase of the NAO when it reaches the North Atlantic. Therefore, the Pr_IOWP forcing is not the main initiator of this abrupt NAO phase reversal. However, together with the Pr_CP forcing, the Pr_IOWP anomaly does contribute to the generation of the positive NAO response during El Niño P1 (Supplementary Fig. 7). This is consistent with previous studies emphasizing the role of the Pr_IOWP in generating the positive NAO response in ENSO early winter^{13–15}.

It is now clear that the ENSO-induced Rossby wave-propagating direction change over the northeastern North American region is important. How this change takes place becomes the next scientific question to be addressed. Because the propagating direction change is confined mostly to the meridional component of the WAF (i.e., F_y), we then decompose this F_y into four terms

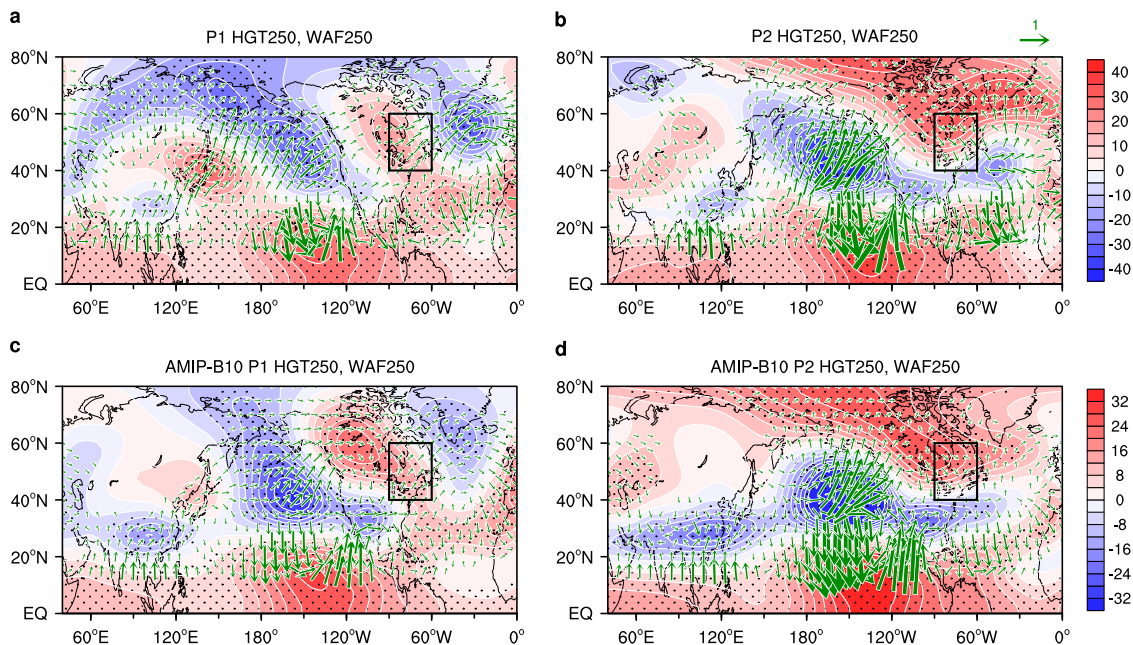


Fig. 2 Change in ENSO-induced Rossby wave-propagating direction leads to the abrupt NAO phase reversal. Regression coefficients of **a, c** P1 and **b, d** P2 250-hPa geopotential height anomalies (shadings and contours in m) with respect to the Niño-3.4 index and the associated wave activity flux (WAF, vectors in m^2s^{-2}) for **a, b** observations and **c, d** the MME of the AMIP-B10 simulations. The black box ($40^\circ\text{--}60^\circ\text{N}$, $60^\circ\text{--}90^\circ\text{W}$) outlines the area that features distinct Rossby wave-propagating directions between P1 and P2. Dots are displayed when the geopotential height anomalies are significant at the 90% confidence level (calculated using a two-tailed Student's *t*-test). The WAF flux is shown only when its magnitude is larger than **a, b** 0.04 and **c, d** 0.02 m^2s^{-2} , respectively.

(see details in Methods) for these two periods, over the target region. The latitudinal distributions of the F_y and its four constituents for P1 and P2 are displayed in Fig. 3a, b. As we can see, F_y over northeastern North America is positive in P1 but negative in P2, which corresponds well with the respective northward and southward WAF propagation in the two periods. Whereas “term 3” and “term 4” are small, “term 1” and “term 2” both show larger amplitudes and are jointly responsible for the F_y anomalies. According to Eq. (2), which is described in Methods, the energy propagation associated with “term 1” and “term 2” respectively depends on $-u/v$ and $-\psi \frac{\partial v}{\partial \phi}$, as the background U at 250-hPa is positive. The $-u/v$ and $-\psi \frac{\partial v}{\partial \phi}$ however, are determined by the horizontal structure of the stream function anomaly. If the anomaly shows an isotropic structure (i.e., $-u/v \approx 0$ and $-\psi \frac{\partial v}{\partial \phi} \approx 0$), the wave energy will hardly propagate meridionally. If the positive anomaly pattern is deformed to have a northwest–southeast tilt, these two terms will be positive (i.e., $-u/v > 0$ and $-\psi \frac{\partial v}{\partial \phi} > 0$) and, therefore, will prompt the Rossby wave energy to head northward. On the contrary, it will propagate southward if the positive anomaly has a northeast–southwest tilt (i.e., $-u/v < 0$ and $-\psi \frac{\partial v}{\partial \phi} < 0$). This is confirmed by the spatial patterns of the ENSO-related atmospheric anomalies over the northeastern North American region (Fig. 2a, b). We indeed observe that the positive geopotential anomalies exhibit a northwest–southeast tilt in P1 but a northeast–southwest tilt in P2. However, why do the atmospheric circulation anomalies over northeastern North America have spatial structures with different

tilting directions in the two periods? This is another scientific question to be resolved.

We assume that this change in the Rossby wave-propagating direction is associated with the atmospheric mean state alteration between the two periods. The climatological distribution of the 250-hPa zonal wind and its spatial change from P1 to P2 are displayed in Fig. 3c. During P1, it shows an evident Atlantic jet over the western Atlantic region, with a central wind speed higher than 40 ms^{-1} . To the north of this Atlantic jet, the westerly wind speed decreases with latitude. The westerly is, therefore, stronger in the south and relatively weaker in the north, over the northeastern North American region. This zonal wind distribution is conducive to forming atmospheric anomalies with a northwest–southeast tilt. From P1 to P2, however, the westerly wind speed accelerates at about 55°N but decelerates at about 40°N . This climatological change weakens the meridional shear of the Atlantic jet on its north edge, which favors tilting of the atmospheric anomaly in a northeast–southwest direction.

To consolidate our hypothesis, we define a zonal wind meridional shear index (U250_shear index) as the climatological zonal wind difference between the regions of $40^\circ\text{--}50^\circ\text{N}$, $60^\circ\text{--}90^\circ\text{W}$, and $50^\circ\text{--}60^\circ\text{N}$, $100^\circ\text{--}120^\circ\text{W}$, which are marked in Fig. 3c. The time evolutions of this U250_shear index and the area-averaged F_y , ‘term 1’ and ‘term 2’ over northeastern North America are displayed in Fig. 3d. It can be seen that all four variables consistently show sharp changes in early January. The U250_shear index first shows a climatological decrease around January 3,

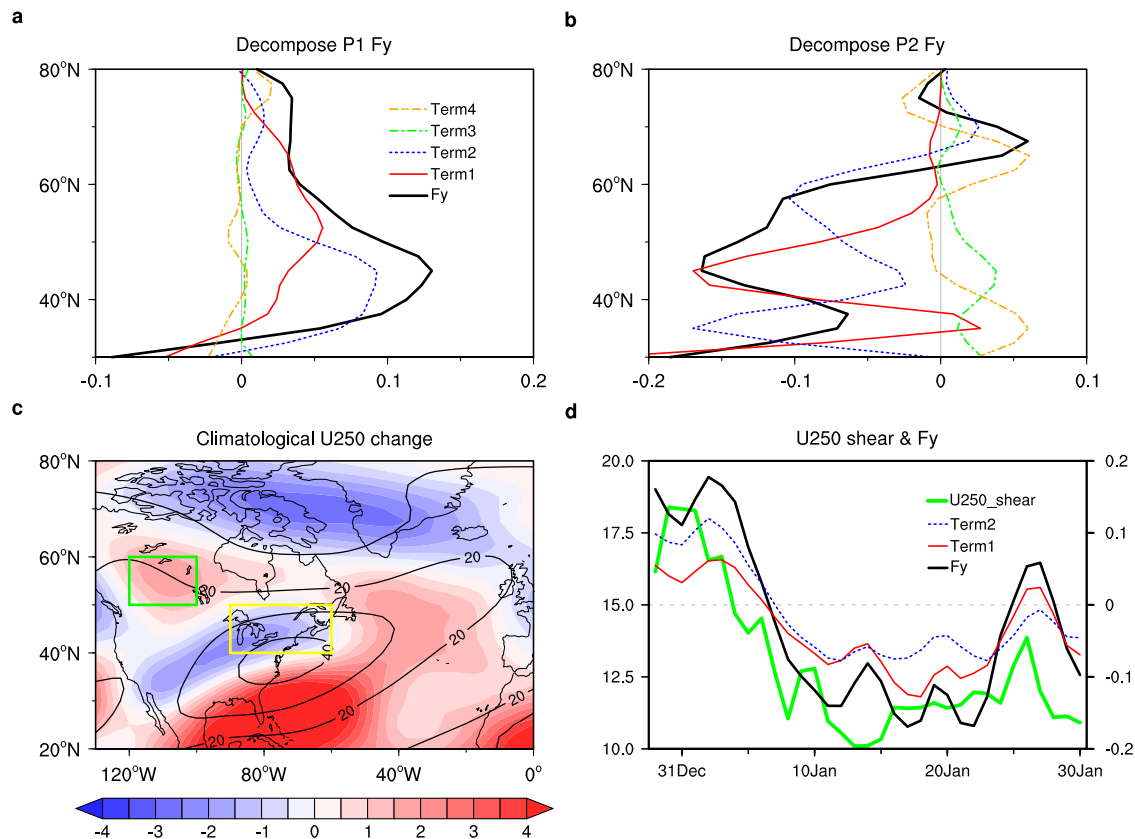


Fig. 3 Climatological alteration of Atlantic jet meridional shear determines the change in Rossby wave-propagating direction. Latitudinal distributions of the meridional component of 250-hPa WAF (F_y) and its four constituents (curves in m^2s^{-2}) with respect to the Niño-3.4 index over the northeastern North American region ($40^\circ\text{--}60^\circ\text{N}$, $60^\circ\text{--}90^\circ\text{W}$) during **a** P1 and **b** P2 for observations. **c** Spatial pattern of climatological 250-hPa zonal wind (contours in ms^{-1}) during P1 for observations. The shadings (units: ms^{-1}) show the corresponding climatological 250-hPa zonal wind differences between P2 and P1. **d** Time evolution of the climatological 250-hPa zonal wind meridional shear index, regression coefficients of F_y , and its two dominant constituents (i.e., “term 1” and “term 2”) with respect to the Niño-3.4 index averaged over the northeastern North American region ($40^\circ\text{--}60^\circ\text{N}$, $60^\circ\text{--}90^\circ\text{W}$) for observations. The yellow ($40^\circ\text{--}50^\circ\text{N}$, $60^\circ\text{--}90^\circ\text{W}$) and green ($50^\circ\text{--}60^\circ\text{N}$, $100^\circ\text{--}120^\circ\text{W}$) boxes in (c) outline the two regions used to define the zonal wind meridional shear (U250_shear) index.

which leads to a significant change of the F_y and its components “term 1” and “term 2” around January 6. As a result, the NAO phase is reversed around January 8. This lead-lag relationship between these three phenomena can be further verified by their time evolution and also by the lead-lag correlations among them (Supplementary Fig. 8). The AMIP simulations also simulate changes in the F_y and its two components, and the associated climatological zonal wind shifts to a large extent (Supplementary Fig. 9). Importantly, the lead-lag relationship between the changes in the climatological zonal wind, F_y , and the NAO phase reversal can also be realistically captured despite slightly different lead-lag days compared to the observations (Supplementary Fig. 10). However, the change in F_y can only explain the negative anomaly in the region of the Iceland during El Niño P1 and in the region of the Azores during El Niño P2, which is only one of the two lobes of the NAO dipolar pattern. The mechanisms responsible for the establishment of the other NAO polarity remain to be elucidated.

It is well known that the NAO is an intrinsic atmospheric mode that is closely involved in local synoptic eddy–low-frequency flow feedback^{34,35}. This strong eddy–low-frequency flow feedback generally follows the “left-hand rule.” In other words, the eddy vorticity fluxes are directed preferentially about 90 degrees toward their left-hand side so that they converge into the cyclonic flow and diverge from the anticyclonic flow^{36,37}. Therefore, if we have negative atmospheric anomalies over the North Atlantic, the eddy vorticity fluxes organized by the cyclonic flow will work to amplify and facilitate the NAO dipolar structure. To confirm this theoretical inference, we display the ENSO-regressed anomalous 250-hPa stream function and eddy vorticity fluxes for P1 and P2 in Fig. 4. The eddy vorticity fluxes indeed follow the “left-hand rule” as they are directed toward the left-hand side of the low-frequency flow. During El Niño P1, the eddy vorticity fluxes converge into the anomalous cyclonic flow at high latitudes. This inevitably leads to a divergence in the south and thus generates a positive stream function anomaly there, which forms a complete positive NAO response. During El Niño P2, the eddy vorticity fluxes converge into the anomalous cyclonic flow in the middle latitudes, which is induced by the Rossby wave trains. This also results in a divergence in the north and thus generates a positive atmospheric anomaly there, which projects onto a completely negative NAO dipolar pattern. The amplifying role played by North Atlantic eddy–low-frequency flow feedback can also be clearly detected in AMIP simulations (Supplementary Fig. 11). Therefore, we suggest that this North Atlantic intrinsic positive synoptic eddy feedback serves as an additional mechanism that facilitates a complete NAO dipolar response during the two periods of ENSO winter. In addition, the presence of such strong positive eddy feedback

helps the NAO phase reversal more sharply than the basic state changes.

DISCUSSION

Previous studies demonstrated that the atmospheric anomalies over the Euro-Atlantic sector are the opposite between early and late ENSO winters. This disparate response is suggested to occur between December and January as the monthly anomalies project onto positive and negative NAO phases, respectively. Despite being widely studied, our understanding of the detailed evolutionary features and physical processes of this signal transition remains immature. In this study, we identify that this NAO phase reversal occurs abruptly and synchronously in early January of ENSO winter. Analyses with regard to the physical mechanisms suggest that the hypotheses proposed by previous studies, including the stratospheric pathway^{18,25,26} and/or the modulation by tropical SST^{21,22} or convection change^{13,14,19}, do not show synchronous influencing signals that can explain the abrupt change in NAO anomalies (Supplementary Figs. 2, 3). This may be because the short-term intraseasonal NAO variability is more immediately driven by tropospheric internal processes^{38,39}, and thus the low-frequency mechanisms may have limitations in capturing the abruptness.

We, therefore, propose a tropospheric mechanism by suggesting that this ENSO–NAO teleconnection reversal stems from an ENSO-induced Rossby wave-propagating direction change, from northeastward to southeastward, before it enters the North Atlantic region. The shift in the propagating direction is associated with the spatial tilt change in the atmospheric perturbations over the northeastern North American region, which in turn is governed by the climatological alteration of the North Atlantic jet meridional shear. We also found that the North Atlantic intrinsic eddy–low-frequency flow feedback works as an amplifier to further facilitate the NAO responses before and after its phase transition.

Our findings have important implications for exploiting the intraseasonal predictability of the NAO and Euro-Atlantic climate associated with ENSO because NAO is the dominant atmospheric mode that affects climate variability in the North Atlantic rim^{31,32}. The results also revealed that ENSO could impact the climate system through extensive interaction with the fast-varying background states. This leads to a frequency cascade in the atmospheric circulation that is characterized by deterministic high-frequency variability⁴⁰. Also, under greenhouse warming, the properties of both ENSO^{41,42} and the Atlantic jet^{43,44} have changed systematically. For example, owing to increased eastern

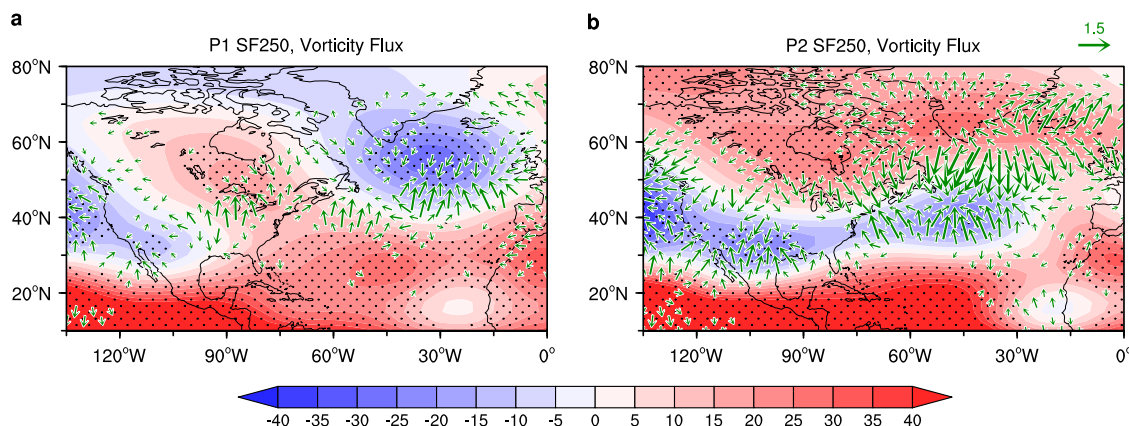


Fig. 4 North Atlantic intrinsic eddy–low-frequency flow feedback further facilitates the NAO dipolar responses. Regression coefficients of **a** P1 and **b** P2 250-hPa geostrophic stream function anomalies (shadings in $10^5 \text{ m}^2 \text{ s}^{-2}$) and eddy vorticity fluxes (vectors in 10^{-5} ms^{-2}) with respect to the Niño-3.4 index for observations. Dots are displayed when the stream function anomalies are significant at the 90% confidence level (calculated using a two-tailed Student’s *t*-test). The eddy vorticity flux is shown only when its magnitude is larger than $0.3 \times 10^{-5} \text{ ms}^{-2}$.

Pacific tropical rainfall variability, the late winter ENSO–NAO teleconnection is suggested to be considerably reinforced in a warmer world^{45,46}. It is, therefore, worthwhile to investigate how this abrupt ENSO–North Atlantic teleconnection reversal in early January responds to a future warming climate.

METHODS

Reanalysis and observational products

The utilized monthly SST datasets (1950–2021) are the National Oceanic and Atmospheric Administration extended reconstructed SST V5 data⁴⁷ with a horizontal resolution of 2° longitude × 2° latitude. Daily SST and precipitation datasets (1950–2021) are derived from the fifth generation of the European Centre for Medium-Range Weather Forecasts reanalysis (ERA-5)⁴⁸ with a horizontal resolution of 1° longitude × 1° latitude. Other daily atmospheric circulations are investigated based on the National Centers for Environmental Prediction/National Center for Atmospheric Research (NCEP/NCAR) reanalysis data⁴⁹ with a horizontal resolution of 2.5° longitude × 2.5° latitude. Anomalies were derived relative to the daily mean climatology over the entire study period (1950–2021). A linear trend was removed to avoid possible influences associated with global warming or long-term trends. We also performed a 9-day running mean to exclude any possible noise disturbances caused by synoptic variability. All statistical significance tests were performed using the two-tailed Student's *t*-test. The NAO index is defined by the difference in normalized SLP anomalies between 35°N and 65°N over the North Atlantic sector (zonally averaged from 80°W to 30°E)⁵⁰. ENSO events are identified based on a threshold of ±0.5 standard deviations of the December to February (DJF) average Niño-3.4 index (averaged SST anomaly in the domain of 5°S–5°N, 120°–170°W). With this method, we can obtain 22 El Niño years: 1953–54, 1957–58, 1958–59, 1963–64, 1965–66, 1968–69, 1972–73, 1976–77, 1977–78, 1979–80, 1982–83, 1986–87, 1987–88, 1991–92, 1994–95, 1997–98, 2002–03, 2004–05, 2006–07, 2009–10, 2015–16, and 2018–19; and 23 La Niña years: 1950–51, 1954–55, 1955–56, 1964–65, 1967–68, 1970–71, 1971–72, 1973–74, 1974–75, 1975–76, 1984–85, 1988–89, 1995–96, 1998–99, 1999–00, 2000–01, 2005–06, 2007–08, 2008–09, 2010–11, 2011–12, 2017–18, and 2020–21. We also tested various thresholds such as ±0.75 or ±1 standard deviations of the Niño-3.4 index to select the ENSO events, and the results are qualitatively consistent.

To determine the relative role of the convection anomalies in the central Pacific and those in the tropical Indo-Western Pacific in the NAO phase reversal, two precipitation indices based on the ENSO-regressed anomalies (Supplementary Fig. 4a) are defined. The tropical Indo-western Pacific index (Pr_IOWP) is defined as the difference between the area-averaged precipitation anomaly in the tropical Indian Ocean (4°S–6°N, 40°–90°E) and the western Pacific (2°–16°N and 110°–150°E). And the tropical central Pacific index (Pr_CP) is defined as the area-averaged precipitation anomaly in the region of 5°S–5°N, 160°E–180°–120°W.

Multi-model CMIP6 simulations

Daily outputs from the 26-model CMIP6 AMIP simulations⁵¹ are utilized to verify and evaluate the atmospheric model responses to observed variations in SST. Details of these models are described in Supplementary Table 1. We analyze the AMIP results from 1979 through to the end of the experiment, in 2014. The horizontal resolutions were interpolated to 2.5° longitude × 2.5° latitude. For each model, only one ensemble member is used, mostly r1i1p1f1, with four exceptions (see details in Supplementary Table 1).

WAF

To analyze the source and direction of energy propagation, the WAF developed by Takaya and Nakamura⁵² is applied. The WAF is parallel to the local group velocity that corresponds to the stationary Rossby waves and is independent of the wave phase⁵². It has been considered a useful tool for supplying information about wave propagation and is defined as

$$F = \frac{p \cos \phi}{2|U|} \left\{ \begin{aligned} & \frac{U}{a^2 \cos^2 \phi} \left[\left(\frac{\partial \psi'}{\partial \lambda} \right)^2 - \psi' \frac{\partial^2 \psi'}{\partial \lambda^2} \right] + \frac{V}{a^2 \cos \phi} \left(\frac{\partial \psi'}{\partial \lambda} \frac{\partial \psi'}{\partial \phi} - \psi' \frac{\partial^2 \psi'}{\partial \lambda \partial \phi} \right) \\ & \frac{U}{a^2 \cos \phi} \left(\frac{\partial \psi'}{\partial \lambda} \frac{\partial \psi'}{\partial \phi} - \psi' \frac{\partial^2 \psi'}{\partial \lambda \partial \phi} \right) + \frac{V}{a^2} \left[\left(\frac{\partial \psi'}{\partial \phi} \right)^2 - \psi' \frac{\partial^2 \psi'}{\partial \phi^2} \right] \end{aligned} \right\} \quad (1)$$

where p is the pressure normalized by 1000 hPa, a is Earth's radius, ϕ is the latitude, and λ is the longitude. The geostrophic stream function ψ is defined as z/f , where z is the geopotential, and f ($= 2\Omega \sin \phi$) is the Coriolis parameter with the Earth's rotation rate (Ω). Also, $|U|$, U , and V represent the basic states of wind speed and zonal and meridional wind, whereas ψ' denotes the perturbed stream function.

To explore the reasons for the changes in the WAF meridional component, we decompose F_y into four components, as follows:

$$\begin{aligned} F_y &= \underbrace{\frac{pU}{2a^2|U|} \frac{\partial \psi'}{\partial \lambda} \frac{\partial \psi'}{\partial \phi}}_{\text{term1}} - \underbrace{\frac{pU}{2a^2|U|} \psi' \frac{\partial^2 \psi'}{\partial \lambda \partial \phi}}_{\text{term2}} + \underbrace{\frac{pV \cos \phi}{2a^2|U|} \left(\frac{\partial \psi'}{\partial \phi} \right)^2}_{\text{term3}} - \underbrace{\frac{pV \cos \phi}{2a^2|U|} \psi' \frac{\partial^2 \psi'}{\partial \phi^2}}_{\text{term4}} \\ &= \underbrace{-\frac{pU \cos \phi}{2|U|} u' v'}_{\text{term1}} - \underbrace{\frac{pU \cos \phi}{2a|U|} \psi' \frac{\partial v'}{\partial \phi}}_{\text{term2}} + \underbrace{\frac{pV \cos \phi}{2|U|} u'^2}_{\text{term3}} + \underbrace{\frac{pV \cos \phi}{2a|U|} \psi' \frac{\partial u'}{\partial \phi}}_{\text{term4}} \end{aligned} \quad (2)$$

Eddy vorticity flux

To obtain the synoptic eddy variability, the daily mean zonal, and meridional winds are bandpass filtered in a period of 2–8 days, using a Lanczos filter (using 41 weights⁵³). The low frequency is defined as the 9-day running mean value. Following previous studies^{36,37}, we define eddy vorticity fluxes as follows to describe the forcing of the synoptic eddies on low-frequency flow:

$$VF = (VF_x, VF_y) = (\overline{u' \zeta'^a}, \overline{v' \zeta'^a}) \quad (3)$$

Here, u' , v' and ζ' denote the bandpass filtered zonal, meridional winds, and vorticity. The overbar represents the 9-day running mean. The superscript, a , indicates the anomaly from the corresponding climatology. The convergence (divergence) of the eddy vorticity flux indicates the cyclonic (anticyclonic) vorticity tendency of the low-frequency flow. Because the rotational component of the eddy vorticity flux does not influence the low-frequency flow, only the divergent component is examined in this study.

Statistical significance test

All our results are tested based on the two-sided Student's *t*-test.

DATA AVAILABILITY

All observational data used in this study are publicly available and can be downloaded from the corresponding websites. ERA5: <https://www.ecmwf.int/en/forecasts/datasets/reanalysis-datasets/era5>; NCEP/NCAR reanalysis: <https://psl.noaa.gov/data/gridded/data.ncep.reanalysis.html>; The CMIP model data used in this study can be obtained from the CMIP6 archives at <https://esgf-node.llnl.gov/search/cmip6/>.

CODE AVAILABILITY

The code for the analysis in this paper is available from the authors upon reasonable request.

Received: 22 December 2022; Accepted: 26 June 2023;
Published online: 07 July 2023

REFERENCES

- McPhaden, M. J., Zebiak, S. E. & Glantz, M. H. ENSO as an integrating concept in Earth science. *Science* **314**, 1740–1745 (2006).
- Ropelewski, C. F. & Halpert, M. S. Global and regional scale precipitation patterns associated with the El Niño/Southern Oscillation. *Mon. Weather Rev.* **115**, 1606–1626 (1987).
- Hoskins, B. J. & Karoly, D. J. The steady linear response of a spherical atmosphere to thermal and orographic forcing. *J. Atmos. Sci.* **38**, 1179–1196 (1981).
- Wallace, J. M. & Gutzler, D. S. Teleconnections in the geopotential height field during the northern hemisphere winter. *Mon. Weather Rev.* **109**, 784–812 (1981).
- Trenberth, K. E. et al. Progress during TOGA in understanding and modeling global teleconnections associated with tropical sea surface temperatures. *J. Geophys. Res.* **103**, 14291–14324 (1998).
- Brönnimann, S. Impact of El Niño–Southern Oscillation on European climate. *Rev. Geophys.* **45**, RG3003 (2007).
- Rogers, J. C. The Association between the North Atlantic Oscillation and the Southern Oscillation in the northern hemisphere. *Mon. Weather Rev.* **112**, 1999–2015 (1984).
- Halpert, M. S. & Ropelewski, C. F. Surface temperature patterns associated with the Southern Oscillation. *J. Clim.* **5**, 577–593 (1992).
- López-Parages, J., Rodríguez-Fonseca, B. & Terray, L. A mechanism for the multidecadal modulation of ENSO teleconnection with Europe. *Clim. Dynam.* **45**, 867–880 (2015).
- Zhang, W. et al. Impact of ENSO longitudinal position on teleconnections to the NAO. *Clim. Dynam.* **52**, 257–274 (2019).
- Moron, V. & Gouirand, I. Seasonal modulation of the El Niño–southern oscillation relationship with sea level pressure anomalies over the North Atlantic in October–March 1873–1996. *Int. J. Climatol.* **23**, 143–155 (2003).
- Ayarzagüena, B., Ineson, S., Dunstone, N. J., Baldwin, M. P. & Scaife, A. A. Intra-seasonal effects of El Niño–Southern Oscillation on North Atlantic climate. *J. Clim.* **31**, 8861–8873 (2018).
- Abid, M. A. et al. Separating the Indian and Pacific Ocean impacts on the Euro-Atlantic response to ENSO and its transition from early to late winter. *J. Clim.* **34**, 1531–1548 (2021).
- Bladé, I., Newman, M., Alexander, M. A. & Scott, J. D. The late fall extratropical response to ENSO: sensitivity to coupling and convection in the tropical West Pacific. *J. Clim.* **21**, 6101–6118 (2008).
- Joshi, M. K., Abid, M. A. & Kucharski, F. The role of an Indian Ocean heating dipole in the ENSO teleconnection to the North Atlantic European region in early winter during the twentieth century in reanalysis and CMIP5 simulations. *J. Clim.* **34**, 1047–1060 (2021).
- King, M. P. et al. Importance of Late Fall ENSO teleconnection in the Euro-Atlantic sector. *Bull. Am. Meteorol. Soc.* **99**, 1337–1343 (2018).
- Thornton, H. E., Smith, D. M., Scaife, A. A. & Dunstone, N. J. Seasonal predictability of the East Atlantic pattern in late autumn and early winter. *Geophys. Res. Lett.* **50**, e2022GL100712 (2023).
- Ineson, S. & Scaife, A. A. The role of the stratosphere in the European climate response to El Niño. *Nat. Geosci.* **2**, 32–36 (2009).
- Jiménez-Esteve, B. & Domeisen, D. I. V. The tropospheric pathway of the ENSO–North Atlantic teleconnection. *J. Clim.* **31**, 4563–4584 (2018).
- Li, R. K. K., Woollings, T., O'Reilly, C. & Scaife, A. A. Effect of the North Pacific tropospheric waveguide on the fidelity of model El Niño teleconnections. *J. Clim.* **33**, 5223–5237 (2020).
- Sung, M.-K., Ham, Y.-G., Kug, J.-S. & An, S.-I. An alternative effect by the tropical North Atlantic SST in intraseasonally varying El Niño teleconnection over the North Atlantic. *Tellus A* **65**, 19863 (2013).
- Ham, Y.-G., Sung, M.-K., An, S.-I., Schubert, S. D. & Kug, J.-S. Role of tropical Atlantic SST variability as a modulator of El Niño teleconnections. *Asia Pac. J. Atmos. Sci.* **50**, 247–261 (2014).
- Li, Y. & Lau, N.-C. Impact of ENSO on the atmospheric variability over the North Atlantic in late winter—role of transient Eddies. *J. Clim.* **25**, 320–342 (2012).
- Manzini, E., Giorgetta, M. A., Esch, M., Kornblueh, L. & Roeckner, E. The influence of sea surface temperatures on the Northern winter stratosphere: ensemble simulations with the MAECHAM5 model. *J. Clim.* **19**, 3863–3881 (2006).
- Cagnazzo, C. & Manzini, E. Impact of the stratosphere on the winter tropospheric teleconnections between ENSO and the North Atlantic and European region. *J. Clim.* **22**, 1223–1238 (2009).
- Bell, C. J., Gray, L. J., Charlton-Perez, A. J., Joshi, M. M. & Scaife, A. A. Stratospheric communication of El Niño teleconnections to European winter. *J. Clim.* **22**, 4083–4096 (2009).

- Iza, M., Calvo, N. & Manzini, E. The stratospheric pathway of La Niña. *J. Clim.* **29**, 8899–8914 (2016).
- Robock, A. El Chinchón eruption: the dust cloud of the century. *Nature* **301**, 373–374 (1983).
- Robock, A. Volcanic eruptions and climate. *Rev. Geophys.* **38**, 191–219 (2000).
- Driscoll, S., Bozzo, A., Gray, L. J., Robock, A. & Stenchikov, G. Coupled model intercomparison project 5 (CMIP5) simulations of climate following volcanic eruptions. *J. Geophys. Res. Atmos.* **117**, D17105 (2012).
- Thompson, D. W. J. & Wallace, J. M. The Arctic oscillation signature in the wintertime geopotential height and temperature fields. *Geophys. Res. Lett.* **25**, 1297–1300 (1998).
- Scaife, A. A., Folland, C. K., Alexander, L. V., Moberg, A. & Knight, J. R. European climate extremes and the North Atlantic oscillation. *J. Clim.* **21**, 72–83 (2008).
- Clarke, A. J. & Van Gorder, S. Improving El Niño prediction using a space-time integration of Indo-Pacific winds and equatorial Pacific upper ocean heat content. *Geophys. Res. Lett.* **30**, 1399 (2003).
- Branstator, G. The maintenance of low-frequency atmospheric anomalies. *J. Atmos. Sci.* **49**, 1924–1946 (1992).
- Ren, H.-L., Jin, F.-F., Kug, J.-S., Zhao, J.-X. & Park, J. A kinematic mechanism for positive feedback between synoptic eddies and NAO. *Geophys. Res. Lett.* **36**, L11709 (2009).
- Kug, J.-S. & Jin, F.-F. Left-hand rule for synoptic eddy feedback on low-frequency flow. *Geophys. Res. Lett.* **36**, L05709 (2009).
- Kug, J.-S., Jin, F.-F., Park, J., Ren, H.-L. & Kang, I.-S. A general rule for synoptic-eddy feedback onto low-frequency flow. *Clim. Dynam.* **35**, 1011–1026 (2010).
- Rivière, G. & Drouard, M. Dynamics of the Northern annular mode at weekly time scales. *J. Atmos. Sci.* **72**, 4569–4590 (2015).
- Gerber, E. P., Orbe, C. & Polvani, L. M. Stratospheric influence on the tropospheric circulation revealed by idealized ensemble forecasts. *Geophys. Res. Lett.* **36**, L24801 (2009).
- Stuecker, M. F., Jin, F.-F. & Timmermann, A. El Niño–Southern Oscillation frequency cascade. *Proc. Natl Acad. Sci. USA* **112**, 13490–13495 (2015).
- Yeh, S.-W. et al. El Niño in a changing climate. *Nature* **461**, 511–514 (2009).
- Cai, W. et al. Increasing frequency of extreme El Niño events due to greenhouse warming. *Nat. Clim. Change* **4**, 111–116 (2014).
- Woollings, T. & Blackburn, M. The North Atlantic jet stream under climate change and its relation to the NAO and EA patterns. *J. Clim.* **25**, 886–902 (2012).
- Simpson, I. R., Shaw, T. A. & Seager, R. A diagnosis of the seasonally and longitudinally varying midlatitude circulation response to global warming. *J. Atmos. Sci.* **71**, 2489–2515 (2014).
- Drouard, M. & Cassou, C. A modeling- and process-oriented study to investigate the projected change of ENSO-forced wintertime teleconnectivity in a warmer world. *J. Clim.* **32**, 8047–8068 (2019).
- Fereday, D. R., Chadwick, R., Knight, J. R. & Scaife, A. A. Tropical rainfall linked to stronger future ENSO–NAO teleconnection in CMIP5 models. *Geophys. Res. Lett.* **47**, e2020GL088664 (2020).
- Huang, B. et al. Extended reconstructed sea surface temperature, version 5 (ERSSTv5): upgrades, validations, and intercomparisons. *J. Clim.* **30**, 8179–8205 (2017).
- Hersbach, H. et al. The ERA5 global reanalysis. *Q. J. R. Meteorol. Soc.* **146**, 1999–2049 (2020).
- Kalnay, E. et al. The NCEP/NCAR 40-year reanalysis project. *Bull. Am. Meteorol. Soc.* **77**, 437–471 (1996).
- Li, J. & Wang, J. X. L. A new North Atlantic oscillation index and its variability. *Adv. Atmos. Sci.* **20**, 661–676 (2003).
- Gates, W. L. AMIP: the atmospheric model intercomparison project. *Bull. Am. Meteorol. Soc.* **73**, 1962–1970 (1992).
- Takaya, K. & Nakamura, H. A formulation of a phase-independent wave-activity flux for stationary and migratory quasigeostrophic eddies on a zonally varying basic flow. *J. Atmos. Sci.* **58**, 608–627 (2001).
- Duchon, C. E. Lanczos filtering in one and two dimensions. *J. Appl. Meteorol. Climatol.* **18**, 1016–1022 (1979).

ACKNOWLEDGEMENTS

This work was supported by the National Research Foundation of Korea (NRF-2022R1A3B1077622 and NRF-2018R1A5A1024958). J.Z. was supported by the National Natural Science Foundation of China (42105022). X.G. was supported by the China Scholarship Council (202008320174). This work was also supported by the National Supercomputing Center with supercomputing resources, and associated technical support (KSC-2021-CHA-0008).

AUTHOR CONTRIBUTIONS

X.G. initiated the idea, prepared all the figures, and wrote the initial draft of the paper. J.-S.K. supervised and improved the whole work, formulated the design of the analyses and figures, and developed the manuscript. J.Z. contributed to the manuscript preparation and provided instructive insights on the analysis.

COMPETING INTERESTS

The authors declare no competing interests.

ADDITIONAL INFORMATION

Supplementary information The online version contains supplementary material available at <https://doi.org/10.1038/s41612-023-00414-2>.

Correspondence and requests for materials should be addressed to Jong-Seong Kug.

Reprints and permission information is available at <http://www.nature.com/reprints>

Publisher's note Springer Nature remains neutral with regard to jurisdictional claims in published maps and institutional affiliations.



Open Access This article is licensed under a Creative Commons Attribution 4.0 International License, which permits use, sharing, adaptation, distribution and reproduction in any medium or format, as long as you give appropriate credit to the original author(s) and the source, provide a link to the Creative Commons license, and indicate if changes were made. The images or other third party material in this article are included in the article's Creative Commons license, unless indicated otherwise in a credit line to the material. If material is not included in the article's Creative Commons license and your intended use is not permitted by statutory regulation or exceeds the permitted use, you will need to obtain permission directly from the copyright holder. To view a copy of this license, visit <http://creativecommons.org/licenses/by/4.0/>.

© The Author(s) 2023